

# *Aedes-AI*: Neural Network Models of Mosquito Abundance

Adrienne C. Kinney<sup>1,\*</sup>, Sean Current<sup>5</sup>, Joceline Lega<sup>2,3,4</sup>

<sup>1</sup> Interdisciplinary Program in Applied Mathematics

<sup>2</sup> Department of Mathematics

<sup>3</sup> Department of Epidemiology and Biostatistics

<sup>4</sup> BIO5 Institute

The University of Arizona, Tucson, AZ, 85721, USA

<sup>5</sup> Department of Computer Science and Engineering

The Ohio State University, Columbus, OH, 43202, USA

\*To whom correspondence should be addressed;

E-mail: akinney1@math.arizona.edu.

November 12, 2021

## Abstract

We present artificial neural networks as a feasible replacement for a mechanistic model of mosquito abundance. We develop a feed-forward neural network, a long short-term memory recurrent neural network, and a gated recurrent unit network. We evaluate the networks in their ability to replicate the spatiotemporal features of mosquito populations predicted by the mechanistic model, and discuss how augmenting the training data with both actual and artificially created time series affects model performance. We conclude with an outlook on how such equation-free models may facilitate vector control or the estimation of disease risk at arbitrary spatial scales.

## 1 Introduction

Artificial Neural Networks (ANNs) are ideally suited for modeling nonlinear, complex phenomena, and have either achieved or surpassed human-level performance on tasks involving image classification, anomaly detection, and event extraction [1, 2, 3, 4]. This manuscript assesses the feasibility of developing ANNs to predict mosquito abundance directly from weather data. To this end, we train, validate, and test different types of neural networks on simulated datasets. Data consists of years of representative daily weather time series for various locations in the US obtained from the Multivariate Adaptive Constructed Analogs (MACA) datasets [5], and of daily mosquito abundance predictions estimated from a mechanistic model, the Mosquito Landscape Simulation (MoLS) [6], which uses the MACA data as

input. We conclude that given 90 days of weather data, artificial neural networks are able to quickly and accurately forecast daily mean mosquito abundance, thereby making it possible to efficiently map mosquito-borne disease risk at any spatial scale, provided corresponding meteorological data are available.

Vector-borne diseases infect hundreds of millions of people annually, disproportionately impacting impoverished communities in tropical areas [7]. The past two decades have seen a surge of outbreaks associated with the vector *Aedes aegypti*, including a 2004 dengue outbreak in Singapore [8], a 2013-2014 chikungunya outbreak in the Americas [9], and the 2014-2015 Zika outbreak in Latin America [10]. These outbreaks exemplify the public health risk of arboviral diseases associated with severe clinical symptoms, but also demonstrate the importance of local vector control efforts to mitigate impact on affected communities [11, 12, 13]. Because vector-borne disease outbreaks require sufficiently high vector populations [14, 15, 12], the ability to predict vector abundance is a central component of assessing disease risk. Forecasting outbreaks is, however, further complicated by global interconnectedness [16] and climate change [17, 18] – factors shown to introduce vectors into previously uninhabited areas and increase the viable range of vectors, respectively.

An ANN-based abundance model is appealing since it could be used as a convenient tool to instantly provide daily forecasts of mosquito abundance. This would allow vector control agencies to plan interventions based on local weather forecasts without requiring the use of computational models like MoLS. Moreover, since *Aedes aegypti* is a known vector for diseases like dengue, chikungunya, and Zika, many studies have provided environment suitability maps for this species and have used them to estimate disease risk (see for instance [16, 19] and references therein). An ANN trained on reproducing MoLS predictions would allow the creation of such maps from a mechanistic abundance model without the need of high power computing typically required to generate the same quantity of predictions using MoLS.

Because artificial neural network predictions often lose accuracy in “unfamiliar” situations, the training data may need to place special emphasis on specific dynamic behaviors that are deemed important by the modeler. Estimating what type and what fraction of additional information is necessary to improve performance plays an important role in the development of ANN-based models. It is these questions that have motivated the work presented in this manuscript. Although they are addressed in the specific context of *Aedes aegypti* abundance, the approaches discussed here are general, and can be extended to other mechanistic models of vector abundance, such as for instance *DyMSim* [20], a model for the abundance of *Culex* species.

## 2 Methods

### 2.1 Training and Input Data

The neural network models discussed in this article have the same input data as MoLS. These consist of daily time series of maximum temperature, minimum temperature, precipitation, and average relative humidity. In MoLS, this information is used to calculate *Aedes aegypti* development, death, and reproductive rates, simulate daily mosquito abundance, and estimate the daily expectation of the number of gravid females [6]. The resulting MoLS

predictions, together with the corresponding input time series, define the training data for the neural network models.

The average lifetime of a mosquito is estimated to be 30 days (about two weeks in immature stages [6] and two weeks in the adult stage [21]). We hypothesize that 90 days, 3 times the average lifespan, is sufficient to capture any correlation between current and future population trends. As a consequence, we train each of the ANN models to forecast daily mosquito abundance given weather data for the prior 90 days.

### 2.1.1 Weather Input Data

We obtain daily weather time series from the Multivariate Adaptive Constructed Analogs (MACA) datasets website [5]. Although we download the entire dataset for 2012-2020, we use daily data for 144 locations in 9 states: Arizona, California, Connecticut, Florida, New Jersey, New York, North Carolina, Texas, and Wisconsin. States other than Arizona are chosen because of their participation in the 2019 CDC *Aedes* Challenge [22] and the locations in this study are the centroids of counties that provided data for the challenge. For Arizona, we use MoLS predictions for the 50 most populated cities in the state. Together, these locations exemplify varying mosquito population patterns associated with different climates: hot and dry summers, hot and humid summers, cold winters, etc. Figure 1 shows the locations whose time series we use for training, validation, and testing of the ANN models.

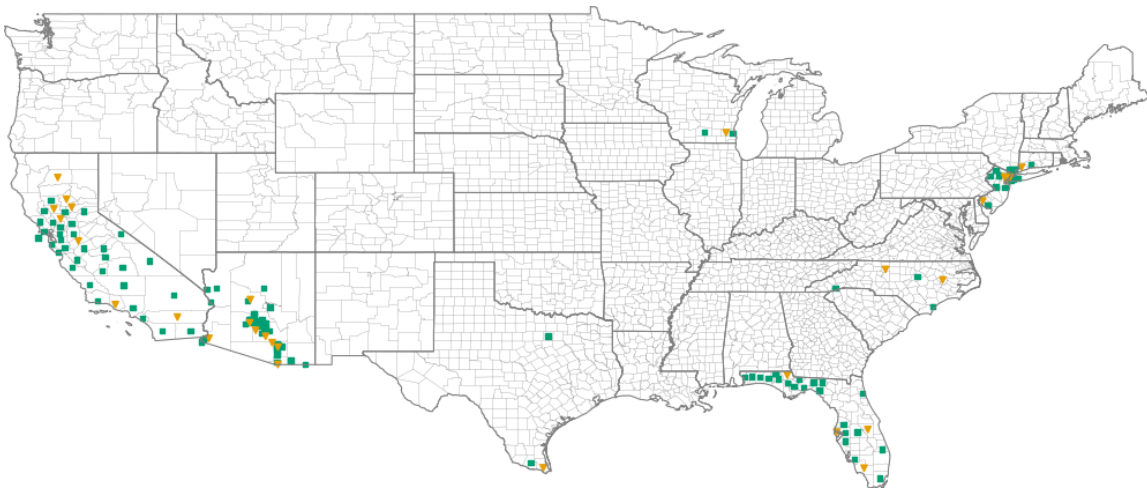


Figure 1: Map of the contiguous United States showing the locations used for training and validation (green squares), and testing (orange triangles). See Tables 13 and 14 in Appendix D for the names of the locations.

### 2.1.2 Mosquito Abundance Input Data

The Mosquito Landscape Simulation (MoLS) is a stochastic agent-based computer simulator for *Aedes aegypti* mosquito populations [6]. MoLS is initiated with a specified number of *Aedes aegypti* eggs, and the simulation follows the life cycle of each egg “laid” in the system.

An egg must survive through five immature stages before emerging as a fertile adult. At each stage in the life cycle, MoLS uses environmental and entomological features to simulate the lifespan of the mosquitoes, including temperature-dependent development rates and gonotrophic cycles, daily survival rates that depend on temperature and relative humidity, precipitation-dependent egg hatching, and carrying capacities estimated from water levels in simulated containers. Although MoLS output includes information on all of the life stages of a mosquito population, its default output is daily scaled gravid female abundance. This allows for direct comparison with surveillance data, which is often collected in gravid mosquito traps. More information about MoLS, including a comparison of its gravid female mosquito predictions against trap data for four neighborhoods in Puerto Rico may be found in [6].

## 2.2 Neural Network Models

We define three neural network models: a feed-forward neural network, a long short-term memory neural network, and a gated recurrent unit neural network. Each model uses one-dimensional convolutional neural networks (1D ConvNet) as a form of feature extraction.

Convolutional neural networks excel in tasks where the input data has a Euclidean, grid-like structure, such as images and time series. We start with a 1D ConvNet to leverage feature extraction resulting from sparsely connected, shared weights. This reduces the number of parameters in the model compared to a fully connected model and facilitates indirect interactions between convolution filters and a larger portion of the input data, allowing the ConvNet to retain information about the temporal structure of the data. Thus, the convolution filters serve as feature extractors and are expected to identify the complex climatic factors that influence *Aedes aegypti* populations. See [23] for a more thorough discussion of convolutional neural networks.

Each of the models used in this study begins with two convolution layers with 64 units each, a kernel size of 3 with no padding, and a stride of 1. Both layers use rectified linear unit (ReLU) activation and are immediately followed by a batch normalization layer as a form of regularization. Batch normalization scales layer outputs according to a learned mean and standard deviation to reduce overfitting and improve generalizability. We consider dropout methods as an alternate means to reduce overfitting, but remove them after they demonstrate no noticeable improvement on the validation set.

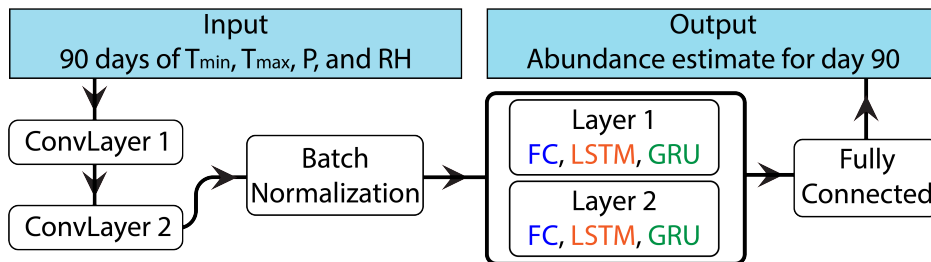


Figure 2: Architecture of the models used in this study.

Figure 2 is a schematic of the architecture used for the models discussed in this article. The layers in the thick-edged box are model dependent: fully-connected (FC) for Model 1, long short-term memory recurrent units (LSTM) for Model 2, and gated recurrent units

(GRU) for Model 3, all of which we describe below. We list the number of trainable parameters for each model in Table 1. Additionally, the reader is referred to Appendix A for details on the layers we use in the models. We discuss the loss function and optimization in §2.3.2.

Model	Trainable Parameters
FF	369,857
LSTM	79,425
GRU	63,297

Table 1: Number of trainable parameters for each of the neural network models.

### 2.2.1 Model 1: Feed-forward convolutional neural network (FF)

The feed-forward network flattens the batch normalization output before applying two fully connected layers and an output layer. The fully connected layers have 64 units and ReLU activation. The output layer is a single unit with ReLU activation and  $\ell_2$  regularization to reduce over-fitting on the training data. The  $\ell_2$  regularization on the output augments the loss function with the  $\ell_2$  norm of the output weights,  $\|w\|_2^2$ , which must be minimized alongside the mean square error (*MSE*) loss. This penalizes large weight terms, requiring the model to utilize multiple features in its decision making, avoiding over-fitting as a result.

### 2.2.2 Model 2: Long short-term memory recurrent neural network (LSTM)

Our second model architecture is an LSTM, chosen to exploit the “memory” feature of recurrent neural networks. LSTM units include gates that selectively allow information to propagate forward, thereby making it possible for previous information to directly influence the model’s behavior. The “memory” feature of LSTMs is relevant for abundance predictions since previous weather patterns impact current populations. For example, significant heat or cold decreases the viability of offspring, limiting future abundance. Moreover, *Aedes aegypti* eggs are known to be resistant to desiccation: long droughts do not necessarily cause a decrease in viable eggs, which can later hatch when rainfall creates new habitat (see for instance [24] and references therein). Whereas ConvNets excel at retaining spatial information, LSTMs dominate sequence prediction tasks and are well suited to pick up on correlation trends in the output data. Thus, for mosquito population predictions, we hypothesize that incorporating LSTM units into a model will increase performance.

The architecture of the LSTM model replaces the two fully connected layers of Model 1 with LSTM layers. Therefore, Model 2 has two LSTM layers, each with 64 units and **tanh** activation. The first LSTM layer returns the sequential values of the LSTM cells at each time step. These values are then input into the second LSTM layer which returns the final state, and is then passed as the input to the final fully connected output layer (see Figure 2).

### 2.2.3 Model 3: Gated recurrent unit recurrent neural network (GRU)

The final model architecture we consider is a GRU, chosen to leverage the benefits of the LSTM model while reducing the number of associated parameters. GRUs, like LSTMs, feature a gated unit to selectively allow information to propagate forward. However, the GRU unit is simpler than a LSTM unit (see Table 1), which reduces training time and the computational cost of using the model to generate predictions.

The GRU architecture is identical to the LSTM architecture, except the LSTM layers are replaced by GRU layers. Thus, Model 3 has two GRU layers, each with 64 units and `tanh` activation. The first GRU layer returns the sequential values of the GRU cells at each time step. These values are then input into the second GRU layer, whose end state serves as input to the final fully connected output layer (Figure 2).

## 2.3 Model Training

### 2.3.1 Data Processing

We define subsets of the data for training, validation, and testing. The training subset contains daily weather data and corresponding MoLS predictions from 2012-2018 for 115 locations, shown in green (squares) in Figure 1, and we use it to set the weights in the ANNs. The validation subset contains data from 2019-2020 of the same 115 locations, and is used during hyperparameter selection (§2.3.2) to optimize model performance. The testing subset contains the daily weather data from 2012-2020 for the 29 locations not included in the training and validation subsets, shown in orange (triangles) in Figure 1. We use the testing subset to evaluate the performance of the optimized models on unseen data.

During the training and validation process of each ANN model, we process the input weather data in samples, where the  $i$ th input sample,  $\mathbf{x}_i \in \mathbb{R}^{90 \times 4}$ , represents 90 consecutive days of daily observations for the four weather variables (precipitation, maximum temperature, minimum temperature, and relative humidity). For each training and validation input sample  $\mathbf{x}_i$ , we define the corresponding output,  $y_i \in \mathbb{R}$ , as the gravid female abundance prediction by MoLS for the 90th day of the input sample. One thousand input samples, and their corresponding outputs, are randomly selected from each location in the training and validation subsets, and randomly shuffled to ensure the model is not dependent on spatiotemporal relationships among successive samples. We scale each sample between 0 and 1 using the minimum and maximum values of each weather variable for the entire training subset before passing them to one of the ANN models. The resulting scaling factors are considered model parameters and are required for processing future weather samples. The training samples are used to optimize the loss function and update the model layer parameters, while the validation samples guide hyperparameter selection, described in §2.3.2.

After the training and validation process, the learned model weights are saved and can be used to make predictions on unseen data. For the testing subset, we again create input samples  $\mathbf{x}_i \in \mathbb{R}^{90 \times 4}$ , scaled between 0 and 1 using the same scaling factors used for the training and validation samples and generate the model abundance prediction for each testing sample.

For each combination of training, validation, and testing location and year, we create an associated abundance curve by constructing a time series of consecutive daily abundance

predictions.

### 2.3.2 Loss Function and Hyperparameter Selection

For each ANN model, the model weight parameters are selected during training by minimizing a loss function, defined as the mean squared error ( $MSE$ ) between model output and MoLS predictions:  $\sum_{i=1}^n (\hat{y}_i - y_i)^2/n$  where  $n$  is the number of data points,  $\hat{y}_i$  is the  $i$ th prediction by the ANN model and  $y_i$  is the  $i$ th prediction by MoLS.

Model hyperparameters include the learning rate  $\alpha$ , first moment decay rate  $\beta_1$ , and the second moment decay rate  $\beta_2$  of the Adam optimizer [25], as well as the number of units and type of activation function for each layer in the model. Given the extensive search space of hyperparameters for neural network models, it is not possible to test all possible combinations of values. We construct each model by initializing layers with few units and iteratively increasing the number of units in each layer until either the desired performance is achieved or diminishing returns on validation performance are observed (“diminishing returns” are defined holistically; in particular, if the increase in the number of weights offers no significant decrease in the validation error after training, the lesser number of weights is used). Activation functions are similarly tested on a layer-by-layer basis. Finally, we test learning rates  $\alpha \in \{0.01, 0.001, 0.0001, 0.00001\}$ . We choose  $\alpha = 0.0001$ , while the first moment decay rate  $\beta_1 = 0.9$  and second moment decay rate  $\beta_2 = 0.999$  of the Adam optimizer are kept at their default values after changes in their values demonstrated less efficient optimization patterns.

We use a batch size of 64 for computational efficiency and 100 epochs with an early stopping patience level of 30 epochs. Early stopping prevents over-fitting the training subset by stopping the training process once no improvement is seen in model performance on the validation subset for 30 epochs. Once the early stopping is triggered, the model parameters for the best performing epoch are selected as the learned weights for the model.

## 2.4 Data Augmentation

The “base” training subset, described in §2.3.1, includes an equal number of input samples from all training locations, but we also define additional training subsets biased towards 1) the double peak pattern observed in hot and dry climates (see Figure 3 *right*) and 2) the absence of mosquito populations during extremely hot and extremely cold periods. We test two data augmentation methods: double peak oversampling supplements the base training subset with additional actual samples, while temperature augmentation introduces artificially generated samples to the base training subset.

### 2.4.1 Double Peak Oversampling (Actual Samples)

The first method we introduce is double peak oversampling (DPO). Here, our goal is to increase the representation of samples featuring the double season pattern (Figure 3 *right*). We manually identify locations in the original training subset featuring the double peak season pattern (see Table 13 in Appendix D), and increase the number of input samples from these locations to 3000, compared to the original 1000 described in §2.3.1. Thus, the DPO training subset includes 3000 randomly chosen input samples from each of the locations

in Table 13 and 1000 randomly chosen input samples from each of the remaining original training locations. By increasing the number of input samples from double peak locations to 3000, we approximately balance the dataset between double peak and single peak locations; of the 115 locations in the training and validation subsets, 29 are labeled as double peak while the remaining 86 locations are single peak. By oversampling double peak locations by a factor of three, we effectively impose a ratio of 1.01:1 of double peak to single peak locations in the training data.

### 2.4.2 Temperature Augmentation (Artificial Samples)

The second approach is temperature augmentation (TA), which involves artificially generating samples designed to teach the models to predict no abundance for extremely hot and extremely cold temperatures. In the original MoLS model, the probability of adult mosquitoes surviving is 0 if the average temperature is below 4°C or above 41°C, see [6]. We randomly select 15,000 of the original 115,000 samples in the base training subset. For the last 21 days of each of the selected samples, we generate a random number between 42°C and the maximum temperature in the training subset, and then shift the maximum and minimum temperatures in the sample such that the average temperature is the randomly selected number. The humidity and precipitation values remain the same, and we set the associated abundance (at the end of the 90-day period covered in the artificial sample) to 0. We repeat this process for extremely cold temperatures; we randomly select 15,000 samples, generate associated random numbers between 3°C and the minimum temperature in the training subset, shift the last 21 days in each sample such that the average temperature is the random number, and set the corresponding abundance to 0. In other words, we create artificial samples by shifting the last 21 days of real temperature data to fall within ranges that are too hot or too cold to support mosquito populations. The 30,000 artificially generated samples are appended to the base training subset to produce the TA training subset.

### 2.4.3 Variant Model Training with Augmented Data

In addition to the DPO and TA training subsets, we define the DPO TA training subset as the combination of the two; the base training subset is supplemented with the actual DPO input samples and the artificial TA input samples. Then we retrain the base models (FF, LSTM, and GRU) using all three new training subsets. We use the same training process as described in §2.3. Thus, in addition to the three base models we have 9 variant models, named according to the combination of base model and training subset: FF DPO, FF TA, FF DPO TA, LSTM DPO, LSTM TA, LSTM DPO TA, GRU DPO, GRU TA, and GR DPO TA.

## 2.5 Post-Processing and Evaluation

As mentioned above, for each 90-day input sample, the neural network models output the number of gravid female mosquitoes expected for the 90th day. We evaluate these models by first generating the 2012-2020 abundance curves for each of the testing locations. We then smooth each time series of daily predictions, and assess both the global and seasonal fit compared to the corresponding MoLS abundance curve.



### 2.5.1 Data Smoothing

Because the output of MoLS is smoothed with two passes of a 15-day moving average filter, we also smooth the constructed time series of ANN predictions before evaluating the performance of these models. We use a Savitzky-Golay filter with a window of 11 and polynomial of order 3 to filter the neural network time series such that the 11 day auto-correlation of the predictions is within 1% of the 11 day auto-correlation of the corresponding MoLS data. The central point of the 3rd order polynomial curve used to fit each 11-day ANN span is returned as the smoothed data point. Any negative values resulting from the smoothing process are set to 0. The reader is referred to [26] for more information on the Savitzky-Golay filter.

### 2.5.2 Global Fit Performance Metrics

We use a range of metrics to assess the performance of the neural network models. These include four metrics that quantify global fit to the MoLS data, as well as four metrics that focus on timing of abundance peaks and season length. These metrics are then combined into a single score that is used to rank the neural network models.

The metrics that quantify global fit to MoLS data are the non-negative coefficient of determination ( $R_+^2$ ), normalized root mean square error ( $NRMSE$ ), relative difference in area under the curve ( $Rel. AUC Diff.$ ), and Pearson correlation ( $r$ ). Specifically, we set

$$R_+^2 = \max \left( 0, 1 - \frac{\sum_{i=1}^n (y_i - \hat{y}_i)^2}{\sum_{i=1}^n (y_i - \bar{y})^2} \right),$$

$$NRMSE = \frac{\sqrt{\sum_{i=1}^n \frac{1}{n} (\hat{y}_i - y_i)^2}}{y_{max} - y_{min}},$$

$$Rel. AUC Diff. = \frac{\sum_{i=2}^n \frac{1}{2} (y_{i-1} + y_i) - \sum_{i=2}^n \frac{1}{2} (\hat{y}_{i-1} + \hat{y}_i)}{\sum_{i=2}^n \frac{1}{2} (y_{i-1} + y_i)},$$

$$r = \frac{\sum_{i=1}^n (y_i - \bar{y})(\hat{y}_i - \hat{y})}{\sqrt{\sum_{i=1}^n (y_i - \bar{y})^2} \sqrt{\sum_{i=1}^n (\hat{y}_i - \hat{y})^2}},$$

where  $n$  is the output sample size,  $y_i$  represents the  $i$ th prediction by MoLS,  $\bar{y}$  is the mean prediction by MoLS over the output sample,  $\hat{y}_i$  is the  $i$ th prediction by the neural network model,  $\hat{y}$  is the associated output sample mean, and  $y_{max} - y_{min}$  is the range of the  $n$  MoLS predictions. While  $R_+^2$  and  $r$  quantify the fit of the predicted abundance curves,  $NRMSE$  and  $Rel. AUC Diff.$  quantify the accuracy of the magnitudes of the predicted abundances. High  $R_+^2$  and  $r$  scores indicate the neural network abundance curves match the shape of the true MoLS curves and low  $NRMSE$  and  $Rel. AUC Diff.$  values indicate the magnitudes of the abundance predictions from the neural network models are similar to the corresponding MoLS abundance predictions. These metrics are computed for output samples of varying

sizes, such as the entire testing output vector ( $n = 100,630$ ) and the output vector for a specific testing location and year ( $n = 365$ ). We use a normalized  $RMSE$  to facilitate comparisons between output samples of different scales (i.e. locations with high mosquito abundance and those with low mosquito abundance) and the non-negative  $R_+^2$  to assign a score of 0 to all low-performing models.

### 2.5.3 Season Feature Performance Metrics: Peak Timing and Season Length

The metrics that quantify peak timing and season lengths are based on the difference, relative to MoLS data, in onset and offset times at various points in the mosquito season for a particular year. Given a threshold  $T$ , we calculate the first day  $i$  the gravid mosquito population  $P_i$  is above the threshold  $T$  for the observed (MoLS) and predicted (by the ANN) data;  $P_i$  is further conditioned that the following 7 days,  $P_{i+1}$  to  $P_{i+7}$ , must also be above the given threshold. We calculate a matching day  $j$  to mark the return to abundance values below  $T$ , which is defined as the first day  $j > i$  such that  $P_j$  and abundance values in the next 7 days are lower than the threshold  $T$ .

Mathematically,  $i$  and  $j$  pairs are defined as follows:

$$i = \min_q \{q : P_{q+\ell} > T \text{ for } \ell = 0, \dots, 7\}$$

$$j = \min_q \{q : P_{q+\ell} < T \text{ for } \ell = 0, \dots, 7 \text{ \& } q > i\}.$$

It is possible that there are multiple sections throughout the year where  $i$  and  $j$  pairs can be generated; this is particularly true for double-peak cities in Arizona and Southern California, where the *Aedes aegypti* population grows initially before dying off in the summer heat, rising again once the temperature cools. In these cases, there is a split season, and the pairs are enumerated as  $(i_k, j_k)_T$  for  $k = 1, \dots, N$ , where  $N$  is the number of regions above the threshold. Regions with  $k = 2, \dots, N$  are constrained such that  $i_k$  must occur after  $j_{k-1}$  ( $j_{k-1} < i_k < j_k$ ).

The pairs  $(i_k, j_k)_T$  are calculated for both the predicted and observed data on a yearly basis. We use the notation  $i_m$  and  $j_m$  to denote onset and offset days for the observed data and  $\hat{i}_n$  and  $\hat{j}_n$  to denote onset and offset days for the predicted data. Each onset day  $i_m$  in the observed data is matched with the nearest onset day  $\hat{i}_n$  in the predicted data, denoted  $\hat{i}_n^m$ , according to the minimum absolute difference of the points. This is mathematically defined as:

$$\hat{i}_n^m = \arg \min_{\hat{i}_n} |\hat{i}_n - i_m|$$

Additionally, predicted days  $\hat{i}_n$  are only allowed to match with a single observed day  $i_m$ . If a predicted day  $\hat{i}_n$  would match with more than one observed day (i.e., there exists  $m_1, m_2$  such that  $\hat{i}_n^{m_1} = \hat{i}_n^{m_2}$ ),  $\hat{i}_n$  is instead only matched to the day  $i_m$  with the minimum absolute difference, and the remaining observed days are matched with the remaining predicted days. This process is similarly done for the offset days  $j_m$  and  $\hat{j}_n$ .

The resulting matchings are used to calculate onset ( $D_{on}$ ) and offset ( $D_{off}$ ) differences as follows

$$D_{on} = \hat{i}_n^m - i_m, \quad D_{off} = \hat{j}_n^m - j_m.$$

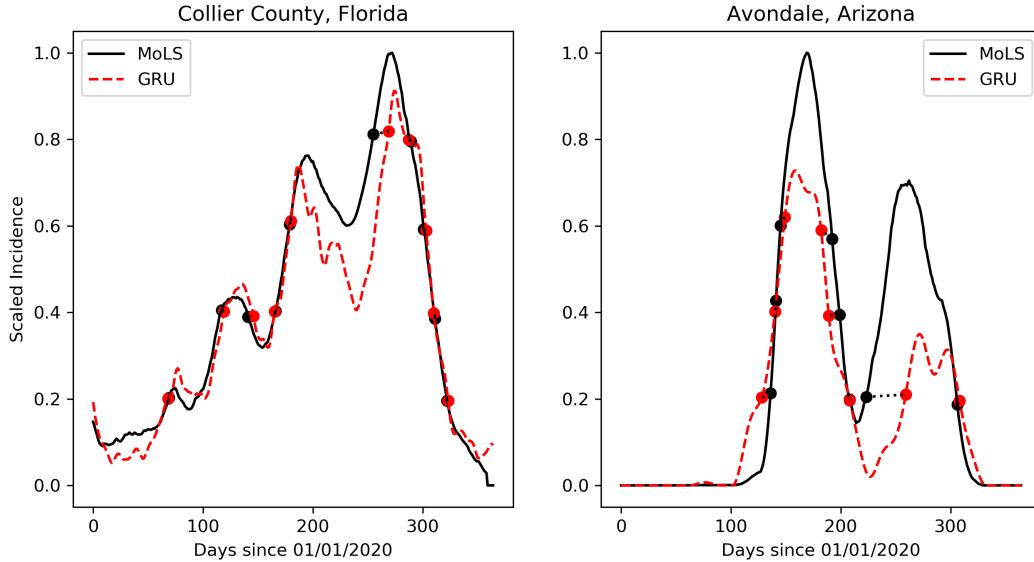


Figure 3: Observed (black solid curve) and predicted (red dashed curve for the GRU model) scaled abundance in Collier County, FL (*left*) and Avondale, AZ (*right*). Each trace is scaled to the peak height of the observed (MoLS) abundance. The dots mark the times when each time series reached 20%, 40%, 60%, and 80% of the maximum MoLS abundance. Points in matching pairs are connected by dotted lines, whose projection on the horizontal axis has length  $D_{on}$  or  $D_{off}$ . Black dots that are not matched to a red dot are omitted in this figure for clarity.

If  $D_{on}$  is negative, the predicted abundance exceeds the threshold  $T$  earlier than MoLS ( $\hat{i}_n^m < i_m$ ), and if  $D_{on}$  is positive, the predicted abundance reaches  $T$  later ( $\hat{i}_n^m > i_m$ ). This is similarly true for  $D_{off}$ . We choose to generate results for thresholds  $T$  that are proportional to the observed data; we test predictions for thresholds at 20%, 40%, 60%, and 80% of the maximum of the MoLS data to capture differences in both peak timing and season length. This process is illustrated in Figure 3 for the GRU model in two locations: Collier County, Florida and Avondale, Arizona.

For a given year, the season length  $\ell_S$  is defined as  $\ell_S = \max(j_m) - \min(i_m)$ . Onsets and offsets are scaled by the average of  $\ell_S$  over the testing years at the given location, to make errors relative to the environment in which they occur; if the location in consideration has a longer average season length, the relative seasonal difference will be lower than the same absolute seasonal difference for a location with a shorter average season length.

For each combination of model, threshold value, and testing location we report the means  $\bar{D}$  and standard deviations  $\sigma(D)$  of  $D_{on}$  and  $D_{off}$  over all years. Additionally, we record the total number of times each neural network model did not reach the selected threshold.

### 2.5.4 Combined Performance Score

For each model and testing location combination, we define a fit-based performance metric

$$d = \left\langle \sqrt{M_1^2 + M_2^2} \right\rangle, \quad M_1 = 1 - (\bar{R}_+^2 \cdot \bar{r})^{1/2}, \quad M_2 = \sqrt{(\overline{Rel. AUC Diff.})^2 + \overline{NRMSE}^2}$$

and a peak and seasonal performance metric

$$h = \frac{1}{Z} \left[ \sum_{i=1}^{N_{th}} (1 + \bar{p}_n(i)) (|\bar{D}_{on}^i| \cdot \sigma(D_{on}^i) + |\bar{D}_{off}^i| \cdot \sigma(D_{off}^i))^{1/2} \right],$$

where  $\bar{*}$  and  $\sigma(*)$  are the mean and standard deviation, respectively, of metric  $*$  calculated over testing years (2012-2020),  $\bar{p}_n(i)$  is the average fraction of times the model did not reach the prescribed threshold,  $Z = \sum_{i=1}^{N_{th}} (1 + \bar{p}_n(i))$  is a normalizing factor, and  $N_{th} = 4$  is the number of thresholds. The mean  $\langle \cdot \rangle$  in  $d$  is calculated over locations in the testing subset. The non-negative coefficient of determination and the Pearson correlation were combined into  $M_1$  as a result of the strong correlation between  $R_+^2$  and  $r$ . The use of terms of the form  $|\bar{D}| \cdot \sigma(D)$  in  $h$  aims to penalize models with large values of  $|\bar{D}_{on}|$  and/or  $|\bar{D}_{off}|$  or large standard deviations. We see some instances where model predictions do not reach the threshold; this is particularly relevant for hot and dry locations at higher thresholds (see, for example, Figure 3 *right*). To calculate  $|\bar{D}|$  and  $\sigma(D)$ , we replace all instances where the model fails to meet a given threshold with the average of  $|D|$  for all location and years at the threshold. The  $1 + \bar{p}_n(i)$  weight then penalizes models that do not always reach all of the prescribed thresholds.

The above information is combined into a single score  $S$ , which can be used to compare different models based on their performance on the testing subset:

$$S = \sqrt{S_1^2 + S_2^2}, \quad S_1 = \frac{d}{\max(d)}, \quad S_2 = \frac{h}{\max(h)},$$

where in each case, the maximum is taken over all combinations of model and location.

## 3 Results

### 3.1 Base Model Performance

During the model development process we use a  $MSE$  loss function to train the model parameters and  $R^2$  accuracy to assess overall performance. As described in §2.3.2, we vary the hyperparameters, mimicking a grid search, until we observe diminishing returns on validation performance. The performance metrics for our trained models with the final selected hyperparameter values are shown in Table 2 for each of the three training, validation, and testing subsets (defined in §2.3.1). The output abundance curves are smoothed according to §2.5.1, and the  $R^2$  and  $RMSE$  metrics for each subset are calculated on the entire output vectors. In particular, the training metrics reflect performance on the entire training subset, even though only 1000 input samples per location were used during the training process (§2.3.1).

Model	Metric	Training	Validation	Testing
FF	$RMSE$	89.536	249.026	233.465
	$R^2$	0.986	0.872	0.913
LSTM	$RMSE$	<b>80.572</b>	180.991	<b>204.883</b>
	$R^2$	<b>0.989</b>	0.932	<b>0.933</b>
GRU	$RMSE$	84.687	<b>173.869</b>	208.530
	$R^2$	0.987	<b>0.938</b>	0.931

Table 2:  $RMSE$  and  $R^2$  metrics for the training, validation, and testing data subsets. The best performing values of  $RMSE$  and  $R^2$  for each subset are in bold.

Table 2 shows that the models perform well at replicating the mosquito abundance predictions of MoLS. The gap between the training and validation performance indicates slight over-fitting to the training subset, but overall the results of training and validation are satisfactory, with  $R^2$  values above 0.98 and 0.87 respectively. Further,  $R^2$  values greater than 0.91 are achieved on the testing subset. While the LSTM model is slightly outperformed by the GRU model on the validation subset, it appears to be the best performing model overall.

In what follows, we provide a detailed analysis of the models performance on the testing subset, using the metrics defined in Sections 2.5.2 through 2.5.4. The results are expected to be representative of what a future user would experience, since they apply to data that was not used during the training and validation process. Table 3 expands on Table 2 and estimates the global fit metrics for the three models. The large standard deviations associated with most of the metrics indicate variability in both the fit ( $R_+^2$ ) and size ( $NRMSE$  and  $Rel. AUC Diff.$ ) of predicted abundance curves. The sample means reported in the  $R_+^2$  column are lower than the  $R^2$  score in Table 2 because the present analysis is performed at a more granular level, for each location and year, rather than over the entire testing subset.

Model	Metric			
	$R_+^2$	$NRMSE$	$Rel. AUC Diff.$	$r$
FF	$0.783 \pm 0.221$	$0.139 \pm 0.075$	$0.033 \pm 0.291$	$0.932 \pm 0.076$
LSTM	<b><math>0.844 \pm 0.162</math></b>	<b><math>0.118 \pm 0.061</math></b>	$0.020 \pm 0.237$	<b><math>0.952 \pm 0.054</math></b>
GRU	$0.823 \pm 0.194$	$0.124 \pm 0.067$	<b><math>-0.014 \pm 0.267</math></b>	$0.948 \pm 0.066$

Table 3: Global fit metrics calculated for the testing subset. The entries for metric  $*$  are formatted as  $\bar{*} \pm \sigma(*)$  where  $\bar{*}$  and  $\sigma(*)$  are the mean and standard deviation calculated over all locations and years. In each column, the entry in bold has the best performing mean. See §2.5.2 for a description of the metrics.

Figure 4 illustrates the nature of this variability in the best (Florida) and worst (Arizona) performing states, based on average metric values. Better and more consistent model performance in Florida than in Arizona suggests higher model accuracy in hot and humid regions when compared to hot and dry regions. The consistency in Florida (small standard deviations for all metrics) and differences between the two states (worse performing mean values associated with larger standard deviations in Arizona) suggest that temporal-variability plays less of a role here than location-variability.

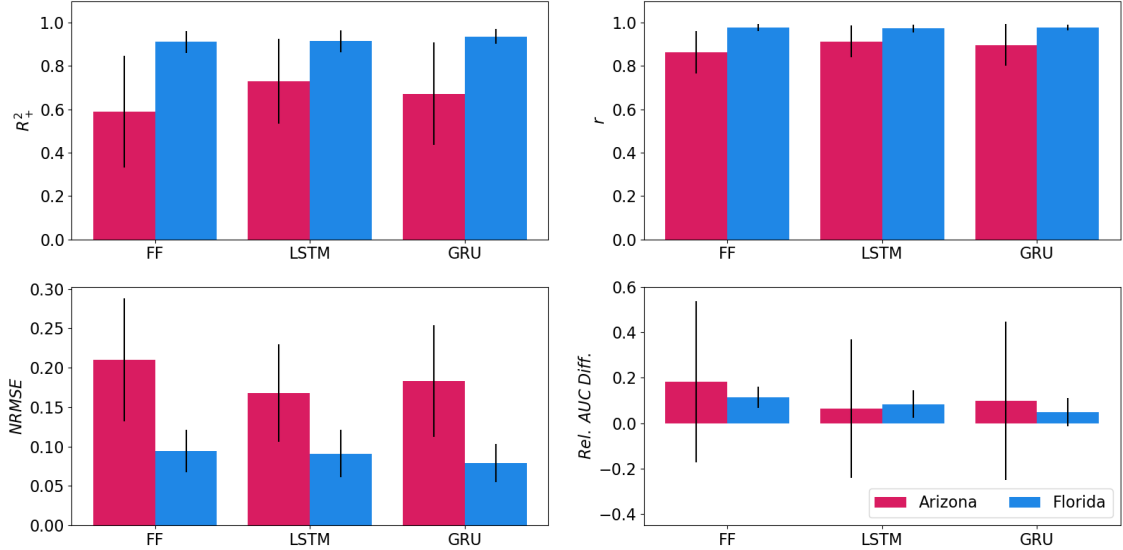


Figure 4: Global fit metrics for Arizona (red, left-hand columns) and Florida (blue, right-hand columns). The thin vertical lines have length equal to two sample standard deviations. In each state, all locations and years available in the testing subset were used. See §2.5.2 for a description of the metrics.

Arizona					
Model	Metric	Threshold (% of Max MoLS Prediction)			
		20%	40%	60%	80%
FF	$D_{on}$	0.008 ± 0.105	-0.056 ± 0.180	-0.080 ± 0.216	<b>0.024 ± 0.132</b>
	$D_{off}$	<b>-0.006 ± 0.061</b>	0.044 ± 0.155	0.046 ± 0.142	0.039 ± 0.193
GRU	$D_{on}$	0.029 ± 0.088	<b>0.014 ± 0.094</b>	-0.037 ± 0.159	-0.025 ± 0.216
	$D_{off}$	-0.033 ± 0.053	<b>0.005 ± 0.116</b>	<b>0.034 ± 0.125</b>	<b>-0.016 ± 0.100</b>
LSTM	$D_{on}$	<b>0.050 ± 0.063</b>	0.031 ± 0.072	<b>-0.015 ± 0.148</b>	0.026 ± 0.175
	$D_{off}$	-0.021 ± 0.056	0.013 ± 0.085	0.054 ± 0.133	0.034 ± 0.160
Florida					
Model	Metric	Threshold (% of Max MoLS Prediction)			
		20%	40%	60%	80%
FF	$D_{on}$	<b>0.006 ± 0.042</b>	-0.021 ± 0.035	-0.055 ± 0.068	-0.061 ± 0.069
	$D_{off}$	<b>0.002 ± 0.023</b>	0.011 ± 0.039	0.040 ± 0.076	0.085 ± 0.123
GRU	$D_{on}$	0.020 ± 0.051	<b>-0.006 ± 0.045</b>	<b>-0.022 ± 0.070</b>	-0.054 ± 0.091
	$D_{off}$	-0.010 ± 0.018	0.006 ± 0.038	0.019 ± 0.056	0.046 ± 0.089
LSTM	$D_{on}$	0.014 ± 0.055	-0.019 ± 0.048	-0.051 ± 0.072	<b>-0.054 ± 0.086</b>
	$D_{off}$	-0.010 ± 0.021	<b>0.001 ± 0.025</b>	<b>0.017 ± 0.050</b>	<b>0.045 ± 0.089</b>

Table 4: Season feature metrics calculated for Arizona and Florida testing locations. Seasonal differences for a location and year are scaled by the average length of the season at the 20% threshold. The entries, formatted as  $\bar{D} \pm \sigma(D)$ , are calculated over all locations and years in each state. Bold entries correspond to the lowest values of  $|D| \cdot \sigma(D)$  for each threshold, with  $D = D_{on}$  or  $D_{off}$ . See §2.5.3 for description of the metrics.

We now turn to the season fit metrics, which explicitly capture deviations in the timing of the predicted season onset, offset, and peaks (see Figure 3). Table 4 shows these metrics for Arizona and Florida; as in Figure 4, averages are taken over all locations and years in each state. While the sample means of  $D_{on}$  and  $D_{off}$  are similar, the standard deviations for Arizona are again much larger than for Florida. In addition, the standard deviations increase with threshold, suggesting that ANNs have more difficulties capturing the timing of peaks (in particular at the 80% threshold) than season onsets and offsets (at the 20% threshold). A similar trend is also observed in the first three rows (above the double line) of Table 11, Appendix B, which shows the means and standard deviations of  $D_{on}$  and  $D_{off}$  over all locations and years in the testing subset.

The above analysis reveals that lower model performance is associated with a lack of ability to capture the timing of abundance peaks. This is particularly true in hot and dry climates, where large temperature differentials are observed. The next section explores whether training the models on augmented data sets that specifically address such variability improves consistency.

### 3.2 Variant Model Performance

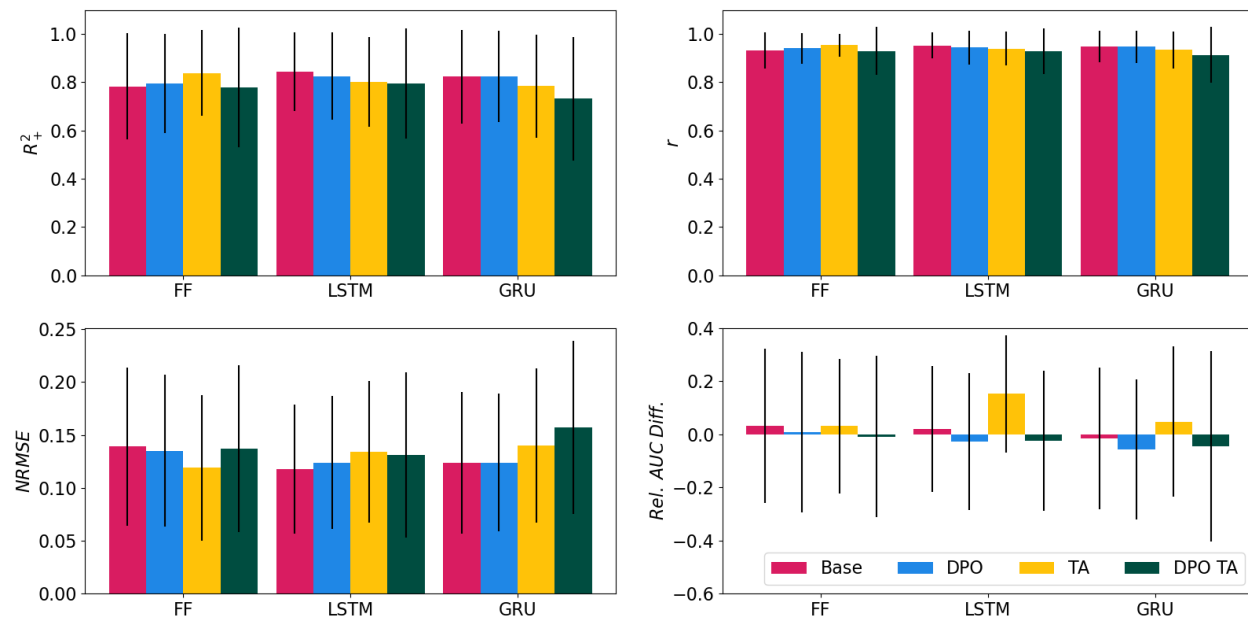


Figure 5: Average performance metrics and standard deviation of the testing locations.

The augmentation methods only lead to improvement in the case of the FF model. Figure 5 shows the global fit metrics, calculated for all locations and years in the testing subset, for all models. The LSTM and GRU base models outperform their variants both in metric values and in consistency. While the FF variants do have better mean values and lower standard deviations than the FF base model, they however do not outperform the LSTM and GRU base models. In addition, large standard deviations are observed for all variants, indicating the data augmentation methods do not improve consistency.

The results of the seasonal feature analysis shown in Appendix B (Table 11), support the conclusions from the global fit metrics. The variant models do not significantly improve seasonal performance, and commonly perform worse than the base models. Further, the base LSTM model consistently performs well for the  $D_{on}$  metric, ranking in the top three models at each threshold. For the  $D_{off}$  metric, no clear winner is apparent.

Appendix C contains a case study of the LSTM variants for Avondale, Arizona and Collier County, Florida. We show the 2020 abundance curves, as well as associated global fit and seasonal feature metrics. The case study exemplifies differences in model variants and overall performance between the two locations.

### 3.3 Comparative Model Performance

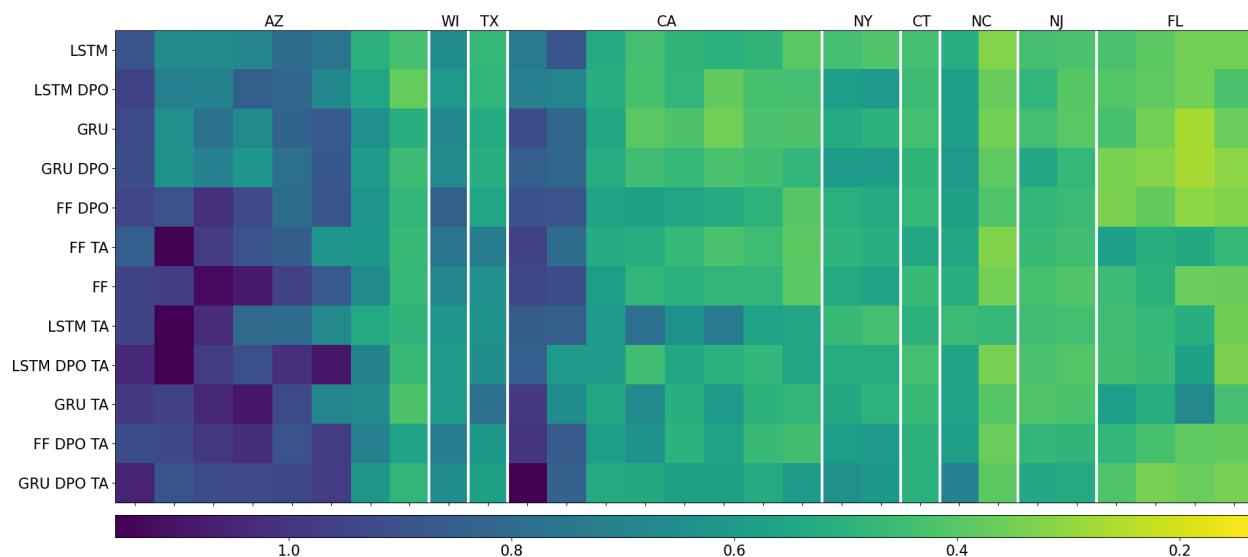


Figure 6: Combined scores on testing locations (see §2.5.4 for metric definition). The rows represent the models and are organized bottom to top from highest score (worst model) to lowest score (best model). The columns represent individual locations (see Table 14 for the names), and the vertical, white lines separate states. The states are organized left to right from highest mean score to lowest, and within each state the locations are organized left to right by descending score.

The overall metric defined in Section 2.5.4 combines the global fit and season feature metrics into a single score. It provides a balanced picture of the performance of each model by taking into account accuracy in terms of season abundance, season length, and peak timing. We show these results in Figure 6. We observe that model architecture impacts performance more than data augmentation; the top four models are difficult to distinguish visually, however, there is a distinct decrease in average model performance starting with the FF DPO model, particularly in Arizona locations.

Also evident from this figure is the significant impact of location on model performance. We see model performance drop for the two left-most locations in California, compared to the rest of the state. Interestingly, these two counties (Ventura County and Riverside County)



are located in the southern portion of the state, whereas the rest of the California locations are in the more humid northern region. All models perform better for locations in humid climates than in dry climates, suggesting the neural networks struggle to identify the role of humidity in abundance predictions. With the exception of Wisconsin, the models perform well for both humid and warm locations and humid and cooler locations, further implicating humidity as a driver of model performance. For reference, the time series for MoLS and the LSTM model used in Figure 6 are provided as supplementary material.

## 4 Discussion

MoLS, a stochastic agent-based model for *Aedes aegypti* abundance that was validated against surveillance data in Puerto Rico [6], uses weather data to simulate the life cycle of a large number of mosquitoes and estimate expected daily abundance. It is natural to ask whether a properly trained artificial neural network is able to “learn” how MoLS combines weather-dependent development, survival, and reproductive rates to make its predictions. In this paper we demonstrate the feasibility of this idea by training ANNs that map meteorological data to mosquito numbers; the 12 models replicate the results of MoLS to varying levels of success, indicating a neural network can function as an equation-free model of *Aedes aegypti* abundance.

While all three base models use the same architecture, shown in Figure 2, incorporating recurrent layers (LSTM and GRU layers) improves performance, compared to the base FF model (Table 2). This suggests that a model using the spatial feature extraction of convolution layers alone is unable to fully identify the relationship between weather features and mosquito abundance, and that combining the sequential “memory” feature of recurrent layers with the convolution layers better captures this relationship.

The impact of data augmentation on model performance is inconclusive. While the LSTM DPO and GRU DPO models slightly underperform the corresponding base models, the FF DPO outperforms its base model. Thus, supplementing the training data with actual, double peak samples seems to emphasize dynamics that the base FF model misses, while the LSTM and GRU models appear to be able to learn such nuances without additional emphasis. Similarly, temperature augmentation helps the base FF model capture previously missed dynamics. However, the LSTM TA and GRU TA variants are significantly worse than their base counterparts (Figure 6). Such a drop in performance suggests the LSTM and GRU models may have learned to recognize the artificial samples and associate them with no abundance rather than learning the intended abundance pattern. In particular, it is possible that adjusting the temperature without also changing the relative humidity created samples that the LSTM and GRU models could identify as artificially generated. A temperature augmentation method that follows §2.4.2, but estimates the relative humidity from the new temperature and precipitation values (using for instance the methods of [27] or [28]), may create believable, artificial samples that better teach the LSTM and GRU models the intended abundance pattern.

Figure 6 demonstrates location-related variability in model performance; all models perform better for locations in humid climates than in dry climates, with good accuracy in both humid and warm locations and humid and cooler locations, except for Wisconsin. But the impact of temporal-related variability is unclear. The difference in performance on the

training and validation subsets likely indicates some overfitting, but may also suggest lower model performance in 2019-2020 compared to 2012-2018. Additional work is therefore required to assess temporal-related variability. To this end, all of our codes are freely available on GitHub to researchers interested in improving on the present results.

Each year of abundance predictions presented in this paper took only 0.33 seconds to generate on a single-processor laptop. The combination of speed and accuracy demonstrated in this article identifies neural network models as top contenders for efficiently converting weather data into *Aedes aegypti* and more generally mosquito abundance. Possible applications of this work therefore include high resolution mapping of disease risk associated with the presence of this vector, both now or as a consequence of climate change, as well as validation of ANN model predictions against mosquito surveillance data.

## Acknowledgements

### Author Contributions

JL conceived of the project and provided the MoLS data. SC led model development efforts and AK led the performance analysis of the models. All authors contributed to the analysis of the results and to the writing of the manuscript. All authors approved the final version of this article.

### Funding

Research reported in this publication was supported in part by the National Institute of General Medical Sciences of the National Institutes of Health under grant GM132008 and by the University of Arizona's BIO5 Institute Team Scholars Program.

### Competing Interests

All authors declare that they have no competing interests.

### Data and Code Availability

All data files, trained models, and codes used to create the figures are available at <https://github.com/T-MInDS/Aedes-AI>

Variable	Description	Dimension/Value	Layers using Variable
$l$	Layer	—	All
$\mathbf{x}_l$	Input for layer $l$	$[n_l \times m_l]$	All
$n_f$	Number of filters	64	ConvLayers
$f$	Filter	$f \in [1, n_f]$	ConvLayers
$\mathbf{K}_f$	Kernel for filter $f$	$[3 \times m_l]$	ConvLayers
$t$	Time index of $x_l$	$t \in [0, n_l)$	All
$\mathbf{O}_l^C$	Output matrix for ConvLayer $l$	$[(n_l - 2) \times 64]$	ConvLayers
$n_u$	Length of hidden state	64	LSTM/GRU Layers
$\mathbf{c}_t$	Cell state at time $t$	$[1 \times n_u]$	LSTM Layers
$\mathbf{h}_t$	Hidden state at time $t$	$[1 \times n_u]$	LSTM/GRU Layers
$\mathbf{f}_t$	Forget gate at time $t$	$[1 \times n_u]$	LSTM Layers
$\mathbf{i}_t$	Input gate at time $t$	$[1 \times n_u]$	LSTM Layers
$\mathbf{o}_t$	Output gate at time $t$	$[1 \times n_u]$	LSTM Layers
$\mathbf{W}_*$	Weight matrix for gate $*$	$[(m_l + n_u) \times n_u]$	LSTM/GRU Layers
$\mathbf{b}_*$	Bias for gate $*$	$[1 \times n_u]$	LSTM/GRU Layers
$\mathbf{r}_t$	Reset gate at time $t$	$[1 \times n_u]$	GRU Layers
$\mathbf{z}_t$	Update gate at time $t$	$[1 \times n_u]$	GRU Layers

Table 5: Variables used in the convolution layers, LSTM layers, and GRU layers. “All” means the variables were used in the three layer types.

## A Description of ANN layers

This appendix provides additional details for the layers used in the neural network models described in §2.2. Note that the parameters appearing in the weight matrices and kernels are learned during the training phase, as described in §2.3. Once trained, the models and their saved parameters may be used for any viable input sample. For a more thorough description of neural networks, we direct readers to [23]. Table 5 shows the variables used in the convolutional layers (ConvLayers), the LSTM layers, and the GRU layers. Each layer is described in more details below.

### A.1 Convolution Layers

Let  $\mathbf{x}_l \in \mathbb{R}^{n_l \times m_l}$  be the input for layer  $l$  and  $\mathbf{K}_f \in \mathbb{R}^{n_K \times m_l}$  be the kernel for filter  $f \in [1, n_f]$ . The dimensions of  $\mathbf{x}_l$  are dependent on layer  $l$ , but the dimensions of  $\mathbf{K}_f$  are constant for all filters  $f$ . In this article,  $n_K = 3$ . Let  $t$  be the time index of the input data such that  $t \in [0, n_l)$ . The output matrix  $\mathbf{O}_l^C \in \mathbb{R}^{(n_l - n_K + 1) \times n_f}$  of convolution layer  $l$  is constructed as follows. For  $t = 0, \dots, (n_l - n_K)$  and  $f = 1, \dots, n_f$ , let  $\hat{\mathbf{x}} = \mathbf{x}_l[t : t + (n_K - 1), :] \in \mathbb{R}^{n_K \times m_l}$  (note that the  $t$  and  $t + (n_K - 1)$  indices are inclusive). Then,  $\mathbf{O}_l^C[t, f] = \sum_{a,b} [\mathbf{K}_f * \hat{\mathbf{x}}]_{a,b}$ , where  $*$  is component-wise multiplication,  $a$  ranges from 0 to  $n_K - 1$ , and  $b$  from 0 to  $m_l - 1$ . Table 6 shows the input and output dimensions for the convolution layers in the models discussed in §2.2.

Layer	Input → Output Dimensions
ConvLayer 1	$[90 \times 4] \rightarrow [88 \times 64]$
ConvLayer 2	$[88 \times 64] \rightarrow [86 \times 64]$

Table 6: Input/output dimensions of the convolution layers used in the models described in §2.2.

## A.2 LSTM Layers

The LSTM layers contain an LSTM unit with hidden state length  $n_u = 64$  and have two sources of information flow:  $\mathbf{C}_t \in \mathbb{R}^{1 \times n_u}$ , the cell state, which intuitively may be thought of as the long-term memory, and  $\mathbf{h}_t \in \mathbb{R}^{1 \times n_u}$ , the hidden state, which is a filtered version of the cell state. Here  $t \in [0, n_l)$ , and  $\mathbf{x}_l \in \mathbb{R}^{n_l \times m_l}$  is the input for the LSTM layer  $l$ . Two of the gates in the unit, the forget gate ( $\mathbf{f}_t \in \mathbb{R}^{1 \times n_u}$ ) and the input gate ( $\mathbf{i}_t \in \mathbb{R}^{1 \times n_u}$ ), selectively update the cell state. The third gate, the output gate ( $\mathbf{o}_t \in \mathbb{R}^{1 \times n_u}$ ), filters the cell state to produce the output, hidden state  $\mathbf{h}_t$ .

The above matrices are constructed as follows. First, the information from the previous hidden state,  $\mathbf{h}_{t-1}$ , is concatenated with the input at time  $t$ ,  $\mathbf{x}_t \in \mathbb{R}^{1 \times m_l}$ , to obtain  $(\mathbf{x}_t \parallel \mathbf{h}_{t-1}) \in \mathbb{R}^{1 \times (m_l + n_u)}$ , where  $(\cdot \parallel \cdot)$  is the concatenation operator. Next, the gates select the information from the concatenation  $(\mathbf{x}_t \parallel \mathbf{h}_{t-1})$  used to update the cell and hidden states. Specifically,  $\mathbf{f}_t = \sigma((\mathbf{x}_t \parallel \mathbf{h}_{t-1})\mathbf{W}_f + \mathbf{b}_f)$ ,  $\mathbf{i}_t = \sigma((\mathbf{x}_t \parallel \mathbf{h}_{t-1})\mathbf{W}_i + \mathbf{b}_i)$ , and  $\mathbf{o}_t = \sigma((\mathbf{x}_t \parallel \mathbf{h}_{t-1})\mathbf{W}_o + \mathbf{b}_o)$ , where  $\sigma$  is the sigmoid activation function and is applied entry-wise. Additionally,  $\tilde{\mathbf{C}}_t$  represents potential information to add to the cell state:  $\tilde{\mathbf{C}}_t = \tanh((\mathbf{x}_t \parallel \mathbf{h}_{t-1})\mathbf{W}_g + \mathbf{b}_g)$ . Here,  $\{\mathbf{W}_f, \mathbf{W}_i, \mathbf{W}_o, \mathbf{W}_g\} \in \mathbb{R}^{(m_l + n_u) \times n_u}$  are the weights of the three gates and potential cell state update, respectively, and  $\{\mathbf{b}_f, \mathbf{b}_i, \mathbf{b}_o, \mathbf{b}_g\} \in \mathbb{R}^{1 \times n_u}$  are the corresponding biases.

Finally, the cell state is updated based on the information from the forget gate and input gate:  $\mathbf{C}_t = \mathbf{f}_t * \mathbf{C}_{t-1} + \mathbf{i}_t * \tilde{\mathbf{C}}_t$ , and the hidden state is produced by filtering the cell state using the output gate:  $\mathbf{h}_t = \tanh(\mathbf{C}_t) * \mathbf{o}_t$ . Here again,  $*$  denotes component-wise multiplication.

See Figure 7a for a pictorial representation of the LSTM unit and Table 7 for the input and output dimensions for the LSTM layers in §2.2. The input layer is the output of a Batch Normalization layer applied to the output of ConvLayer 2 from Table 6. In LSTM Layer 1, the sequential hidden states,  $\mathbf{h}_t$ , are returned for each time step  $t \in [0, n_l)$ , whereas in LSTM Layer 2 only the final hidden state  $\mathbf{h}_t$  is returned, where  $t = n_l - 1$ .

Layer	Input → Output Dimensions
LSTM Layer 1	$[86 \times 64] \rightarrow [86 \times 64]$
LSTM Layer 2	$[86 \times 64] \rightarrow [1 \times 64]$

Table 7: Input/output dimensions of the LSTM layers used in §2.2.

## A.3 GRU Layers

GRU layers each have a GRU unit with hidden state length  $n_u = 64$  and gated structures to selectively allow information to propagate. In the GRU unit,  $\mathbf{h}_t \in \mathbb{R}^{1 \times n_u}$  represents the

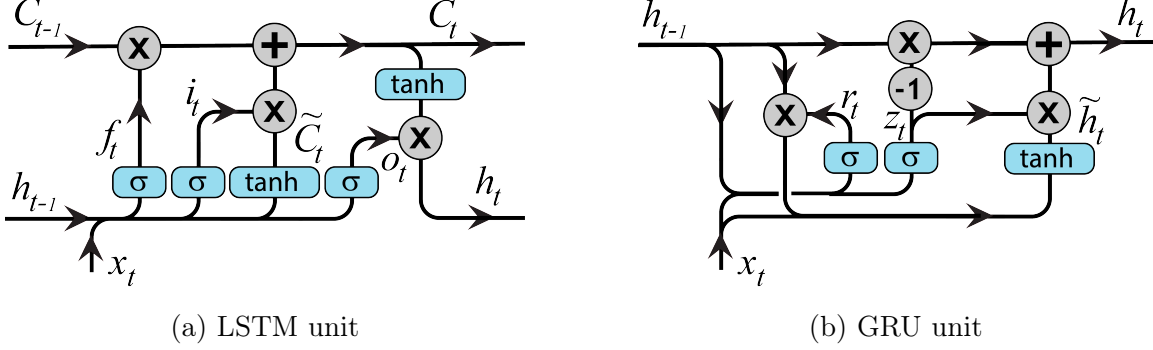


Figure 7: The recurrent units in the LSTM (*left*) and GRU (*right*) layers.

hidden state. The reset gate,  $\mathbf{r}_t \in \mathbb{R}^{1 \times n_u}$ , controls the amount of previous information to include in the hidden state and the update gate,  $\mathbf{z}_t \in \mathbb{R}^{1 \times n_u}$ , selectively adds new information to the hidden state.

Mathematically, the gates are structured similarly to the LSTM gates. First, the input at time step  $t$ ,  $\mathbf{x}_t \in \mathbb{R}^{1 \times m_l}$  is concatenated with the previous hidden state,  $(\mathbf{x}_t \parallel \mathbf{h}_{t-1}) \in \mathbb{R}^{1 \times (m_l + n_u)}$ . Next the gates select the information from the concatenation to be used to update the hidden state:  $\mathbf{r}_t = \sigma((\mathbf{x}_t \parallel \mathbf{h}_{t-1})\mathbf{W}_r + \mathbf{b}_r)$  and  $\mathbf{z}_t = \sigma((\mathbf{x}_t \parallel \mathbf{h}_{t-1})\mathbf{W}_z + \mathbf{b}_z)$  where  $\{\mathbf{W}_r, \mathbf{W}_z\} \in \mathbb{R}^{(m_l + n_u) \times n_u}$  and  $\{\mathbf{b}_r, \mathbf{b}_z\} \in \mathbb{R}^{1 \times n_u}$  are the weights and biases of  $\mathbf{r}_t$  and  $\mathbf{z}_t$ , respectively.

Next,  $\tilde{\mathbf{h}}_t$  is created to represent the potential information to add to the hidden state:  $\tilde{\mathbf{h}}_t = \tanh((\mathbf{x}_t \parallel (\mathbf{h}_{t-1} * \mathbf{r}_t))\mathbf{W}_h + \mathbf{b}_h)$  where  $\mathbf{W}_h \in \mathbb{R}^{(m_l + n_u) \times n_u}$  and  $\mathbf{b}_h \in \mathbb{R}^{1 \times n_u}$  are the weight and biases of the potential hidden state,  $\tilde{\mathbf{h}}_t$ , and  $*$  is component-wise multiplication. Finally, the hidden state is updated by weighting the potential information to add to the hidden state and the previous hidden state:  $\mathbf{h}_t = \mathbf{z}_t * \tilde{\mathbf{h}}_t + (1 - \mathbf{z}_t) * \mathbf{h}_{t-1}$ .

See Figure 7b for a pictorial representation of the GRU unit and Table 8 for the input and output dimensions for the GRU layers in §2.2. Like the LSTM layers, the input layer is the output of a Batch Normalization layer applied to the output of ConvLayer 2 from Table 6. In GRU Layer 1 the sequential hidden states  $\mathbf{h}_t$  are returned for  $t \in [0, n_{x_l})$ , whereas in GRU Layer 2 only the final hidden state  $\mathbf{h}_t$  is returned for  $t = n_{x_l} - 1$ .

Layer	Input $\rightarrow$ Output Dimensions
GRU Layer 1	$[86 \times 64] \rightarrow [86 \times 64]$
GRU Layer 2	$[86 \times 64] \rightarrow [1 \times 64]$

Table 8: Input/output dimensions of the GRU Layers used in §2.2.

#### A.4 Fully Connected Layers and Output Layers

For fully connected (FC) layer  $l$ , let  $\mathbf{x}_l \in \mathbb{R}^{1 \times (n_l \cdot m_l)}$  represent the input. Then the output of  $l$ ,  $\mathbf{O}_l^{FC} \in \mathbb{R}^{1 \times n_{fc}}$ , is:  $\mathbf{O}_l^{FC} = \sigma(\mathbf{x}_l \mathbf{W} + \mathbf{b})$  for weight matrix  $\mathbf{W} \in \mathbb{R}^{(n_l \cdot m_l) \times n_{fc}}$ , bias  $\mathbf{b} \in \mathbb{R}^{1 \times n_{fc}}$ , and specified output dimension  $n_{fc} \in \mathbb{N}^+$ , where  $\sigma$  is the ReLU activation function applied entry-wise.

In Model 1 (FF) we have two fully connected layers with  $n_{fc} = 64$ . Table 9 shows the input and output dimensions for the feed forward layers in §2.2.

<b>Layer</b>	<b>Input → Output Dimensions</b>
FF 1	$[1 \times 5504] \rightarrow [1 \times 64]$
FF 2	$[1 \times 64] \rightarrow [1 \times 64]$

Table 9: Input/output dimensions of the FC Layers used in §2.2.

The last layer for all three models is a fully connected output layer with  $n_{fc} = 1$ , shown in Table 10.

<b>Layer</b>	<b>Input → Output Dimensions</b>
FC Output	$[1 \times 64] \rightarrow [1 \times 1]$

Table 10: Input/output dimensions of the FC output layers used in §2.2.

## B Seasonal feature analysis of all models

Here we provide additional results mentioned in §3.1, which support the conclusion that the base models generally perform better than their variants.

Model	Metric	Threshold (% of Max MoLS Prediction)			
		20%	40%	60%	80%
FF	$D_{on}$	$0.057 \pm 0.113$	<b><math>0.013 \pm 0.133</math></b>	$-0.019 \pm 0.162$	<b><math>0.008 \pm 0.132</math></b>
	$D_{off}$	$-0.006 \pm 0.059$	$0.012 \pm 0.107$	$0.021 \pm 0.118$	$0.01 \pm 0.135$
LSTM	$D_{on}$	<b><math>0.059 \pm 0.077</math></b>	$0.035 \pm 0.097$	$-0.003 \pm 0.119$	$-0.011 \pm 0.141$
	$D_{off}$	$-0.016 \pm 0.056$	<b><math>0.003 \pm 0.08</math></b>	$0.026 \pm 0.116$	$0.003 \pm 0.115$
GRU	$D_{on}$	$0.061 \pm 0.088$	$0.041 \pm 0.095$	$0.009 \pm 0.128$	$0.009 \pm 0.137$
	$D_{off}$	$-0.032 \pm 0.058$	$-0.007 \pm 0.09$	<b><math>0.002 \pm 0.096</math></b>	$-0.009 \pm 0.105$
FF DPO	$D_{on}$	$0.059 \pm 0.094$	$0.034 \pm 0.094$	$-0.001 \pm 0.134$	$0.015 \pm 0.136$
	$D_{off}$	<b><math>0.002 \pm 0.08</math></b>	$0.013 \pm 0.116$	$0.02 \pm 0.128$	$-0.005 \pm 0.133$
FF TA	$D_{on}$	$0.077 \pm 0.09$	$0.056 \pm 0.104$	$0.027 \pm 0.127$	$0.03 \pm 0.153$
	$D_{off}$	$-0.006 \pm 0.085$	$0.016 \pm 0.135$	$0.047 \pm 0.164$	$0.003 \pm 0.154$
FF DPO TA	$D_{on}$	$0.052 \pm 0.104$	$0.032 \pm 0.111$	$0.008 \pm 0.136$	$0.025 \pm 0.145$
	$D_{off}$	$-0.015 \pm 0.08$	$0.002 \pm 0.128$	$0.025 \pm 0.164$	$-0.034 \pm 0.157$
LSTM DPO	$D_{on}$	$0.064 \pm 0.082$	$0.045 \pm 0.096$	$0.006 \pm 0.145$	$0.023 \pm 0.125$
	$D_{off}$	$-0.027 \pm 0.063$	$-0.016 \pm 0.052$	$0.004 \pm 0.082$	<b><math>-0.003 \pm 0.103</math></b>
LSTM TA	$D_{on}$	$0.071 \pm 0.093$	$0.039 \pm 0.113$	<b><math>0.001 \pm 0.129</math></b>	$0.016 \pm 0.143$
	$D_{off}$	$-0.01 \pm 0.114$	$0.03 \pm 0.146$	$0.052 \pm 0.144$	$0.031 \pm 0.131$
LSTM DPO TA	$D_{on}$	$0.068 \pm 0.091$	$0.047 \pm 0.101$	$0.009 \pm 0.155$	$0.027 \pm 0.152$
	$D_{off}$	$-0.018 \pm 0.124$	$0.016 \pm 0.177$	$0.002 \pm 0.132$	$-0.022 \pm 0.129$
GRU DPO	$D_{on}$	$0.073 \pm 0.085$	$0.052 \pm 0.099$	$0.02 \pm 0.124$	$0.014 \pm 0.127$
	$D_{off}$	$-0.038 \pm 0.052$	$-0.025 \pm 0.076$	$-0.006 \pm 0.104$	$-0.016 \pm 0.105$
GRU TA	$D_{on}$	$0.072 \pm 0.099$	$0.035 \pm 0.114$	$0.008 \pm 0.142$	$0.028 \pm 0.134$
	$D_{off}$	$-0.011 \pm 0.106$	$0.03 \pm 0.15$	$0.042 \pm 0.154$	$0.005 \pm 0.13$
GRU DPO TA	$D_{on}$	$0.072 \pm 0.088$	$0.054 \pm 0.085$	$0.016 \pm 0.116$	$0.014 \pm 0.133$
	$D_{off}$	$-0.03 \pm 0.068$	$-0.016 \pm 0.091$	$0.005 \pm 0.108$	$-0.007 \pm 0.111$

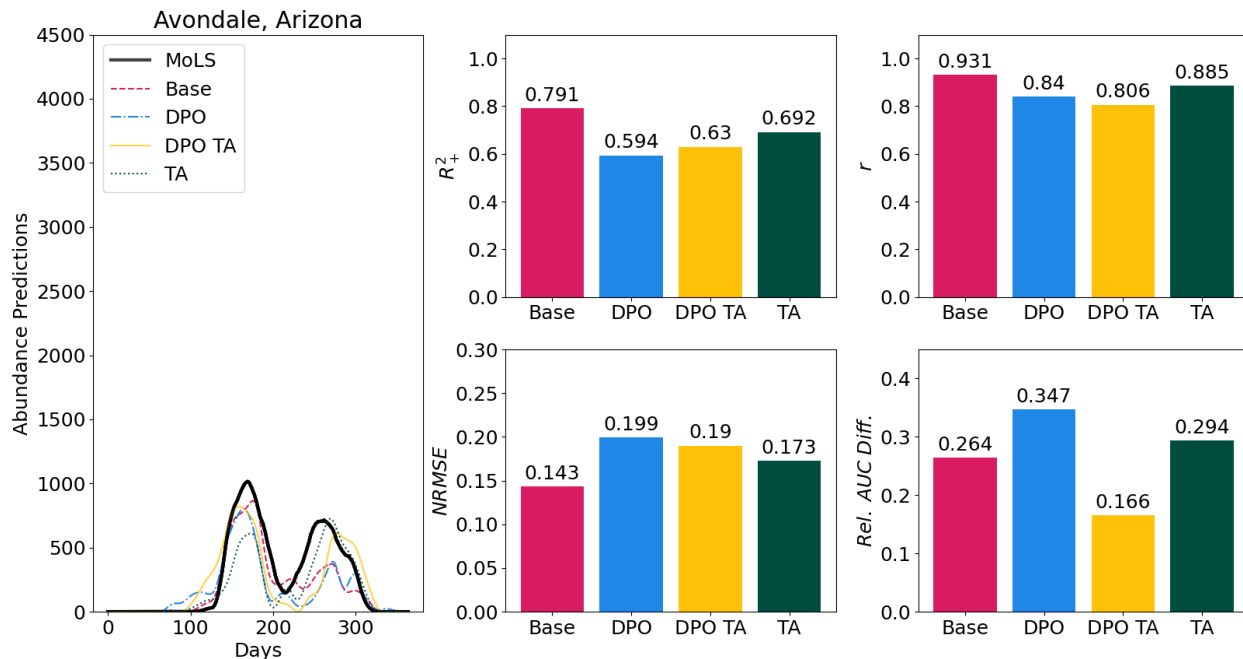
Table 11: Seasonal feature metrics for the testing subset. The double line separates the base models (top three rows) from the variant models (below). Seasonal differences for a location are scaled by the average length of the season at the 20% threshold. Entries are formatted as  $\bar{D} \pm \sigma(D)$  and bold entries correspond to the lowest values of  $|\bar{D}| \cdot \sigma(D)$  for each threshold, with  $D = D_{on}$  or  $D_{off}$ . See §2.5.3 for a description of the metrics.

## C Case Study

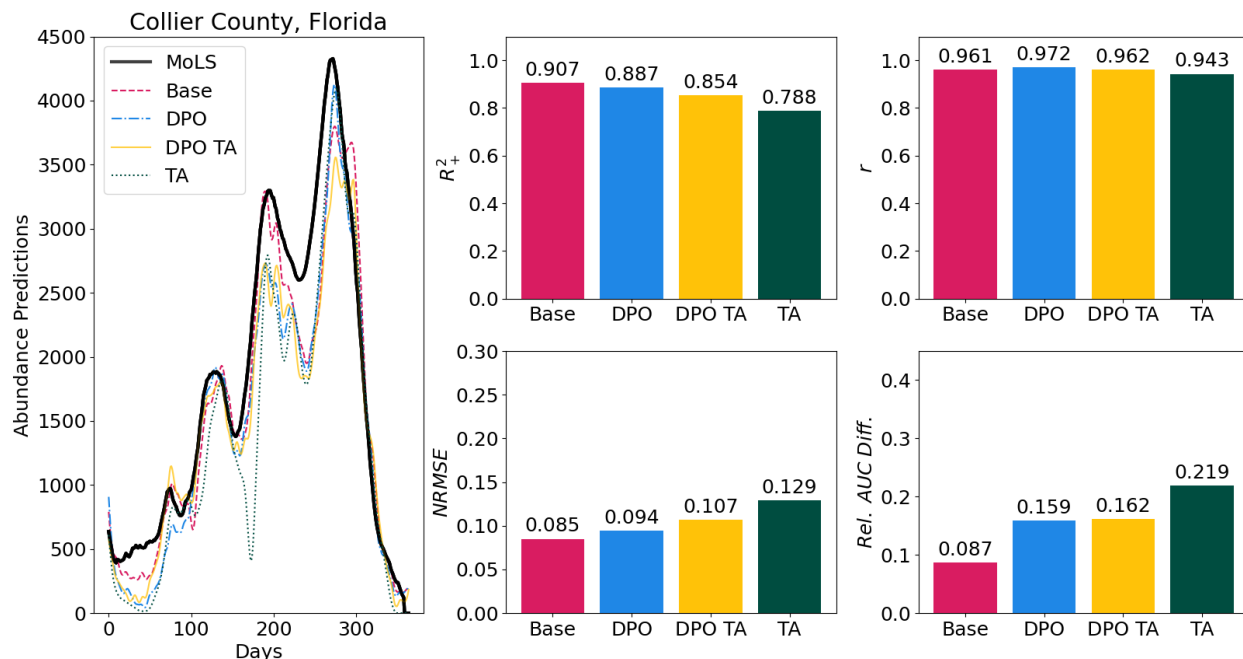
We present an analysis of the base LSTM and LSTM variant models for Avondale, Arizona and Collier County, Florida to illustrate the differences in performance observed among the model archetypes and across different climate regions. Figures 8a and 8b compare the MoLS abundance to the predictions of the ANN models for the year 2020. Abundance curves are on the left and associated global fit metrics are on the right. Such a juxtaposition brings visual context to differences in metric values and trends observed in the main sections of the article: the base LSTM model outperforms LSTM variants and overall model performance is better in Collier County, Florida than in Avondale, Arizona.

Tables 12a and 12b illustrate how the metrics behave for seasons of different lengths and shapes. In Collier County we see one long season, whereas in Avondale there are two distinct peaks (reported metrics are the average of the two). The LSTM DPO TA model fails to meet the 80% threshold in both locations, while the LSTM DPO model fails to meet the 80% threshold for Avondale, Arizona and the LSTM TA model fails to meet the 80% threshold for Collier County, Florida. Values of  $D_{on}$  and  $D_{off}$  are scaled to the season length  $l_S$ . Thus, for  $D_{on}$  at the 80% threshold, the base LSTM model is off by an average of  $10\% \cdot 165.5 \approx 17$  days in Avondale, Arizona and by  $4.3\% \cdot 276.6 \approx 12$  days in Collier County, Florida.





(a)



(b)

Figure 8: The predicted 2020 abundance curves for the LSTM model variants and associated performance metrics for (a) Avondale, Arizona and (b) Collier County, Florida. The base LSTM abundance curve has the best scores in 3 of the 4 metrics for each location (highest  $R^2$  and  $r$  values, and lowest  $NRMSE$  and  $Rel. AUC Diff.$  values), indicating it is the top performing model for both locations. The reader is referred to §2.5.2 for descriptions of the metrics.

Model	Metric	Threshold (% of Max MoLS Prediction)			
		20%	40%	60%	80%
Base	$\bar{D}_{on}$	-0.057	0	-0.012	-0.1
	$\bar{D}_{off}$	-0.009	0.042	0.030	0.006
DPO	$\bar{D}_{on}$	-0.1	0.006	-0.018	-
	$\bar{D}_{off}$	0.048	0.085	0.085	-
TA	$\bar{D}_{on}$	-0.069	0.006	-0.012	-0.018
	$\bar{D}_{off}$	0.118	0.060	0.054	0.091
DPO TA	$\bar{D}_{on}$	-0.06	-0.082	0.012	-
	$\bar{D}_{off}$	0.054	0.076	0.109	-

(a) 2020 Avondale, Arizona. Season length  $\ell_S = 165.5$

Model	Metric	Threshold (% of Max MoLS Prediction)			
		20%	40%	60%	80%
Base	$D_{on}$	-0.033	-0.033	-0.007	-0.043
	$D_{off}$	-0.009	0.042	0.03	0.006
DPO	$D_{on}$	-0.029	-0.018	-0.025	-0.043
	$D_{off}$	-0.004	-0.002	-0.011	0.014
TA	$D_{on}$	-0.007	-0.034	-0.014	—
	$D_{off}$	-0.007	0.005	0.343	—
DPO TA	$D_{on}$	-0.416	-0.011	-0.007	—
	$D_{off}$	-0.007	0.005	0.343	—

(b) 2020 Collier County, Florida. Season length  $\ell_S = 276.6$

Table 12: Season feature metrics for (a) Avondale, Arizona and (b) Collier County, Florida. Blank entries represents instances where the model failed to meet the given threshold. Seasonal differences for a location and year are scaled by the average length of the season at the 20% threshold. See §2.5.3 for description of the metrics.

## D Locations used in the training, validation, and testing subsets

State	Training/Validation Locations
Arizona (Cities)	Anthem*, Apache Junction*, Buckeye*, Bullhead City*, Casa Grande*, Casas Adobes, Catalina Foothills, Chandler*, Douglas, Drexel Heights, El Mirage*, Flagstaff, Florence*, Flowing Wells, Fountain Hills*, Gilbert*, Glendale*, Goodyear*, Green Valley, Kingman, Lake Havasu City*, Mesa*, New River*, Oro Valley, Paradise Valley*, Payson, Peoria*, Phoenix*, Prescott, Queen Creek*, Rio Rico, Sahuarita, San Luis*, San Tan Valley*, Scottsdale*, Sierra Vista, Somerton*, Sun City*, Surprise*, Tanque Verde, Tempe*, Yuma*
California (Counties)	Alameda, Contra Costa, Fresno, Glenn, Imperial*, Inyo, Kern, Kings, Lake, Los Angeles, Madera, Marin, Merced, Mono, Monterey, Napa, Orange, Placer, Sacramento, San Benito, San Bernardino*, San Diego, San Joaquin, San Luis Obispo, San Mateo, Santa Barbara, Santa Clara, Santa Cruz, Solano, Sonoma, Sutter, Tulare
Connecticut (Counties)	New Haven
Florida (Counties)	Calhoun, Escambia, Gadsden, Hillsborough, Holmes, Jefferson, Lee, Liberty, Madison, Manatee, Martin, Miami-Dade, Okaloosa, Pasco, Polk, Santa Rosa, St. Johns, Taylor, Wakulla, Walton, Washington
New Jersey (Counties)	Cumberland, Mercer, Monmouth, Morris, Sussex, Warren
New York (Counties)	Bronx, Kings, Nassau, Queens, Rockland, Westchester
North Carolina (Counties)	New Hanover, Transylvania, Wake
Texas (Counties)	Hidalgo, Tarrant
Wisconsin (Counties)	Dane, Milwaukee

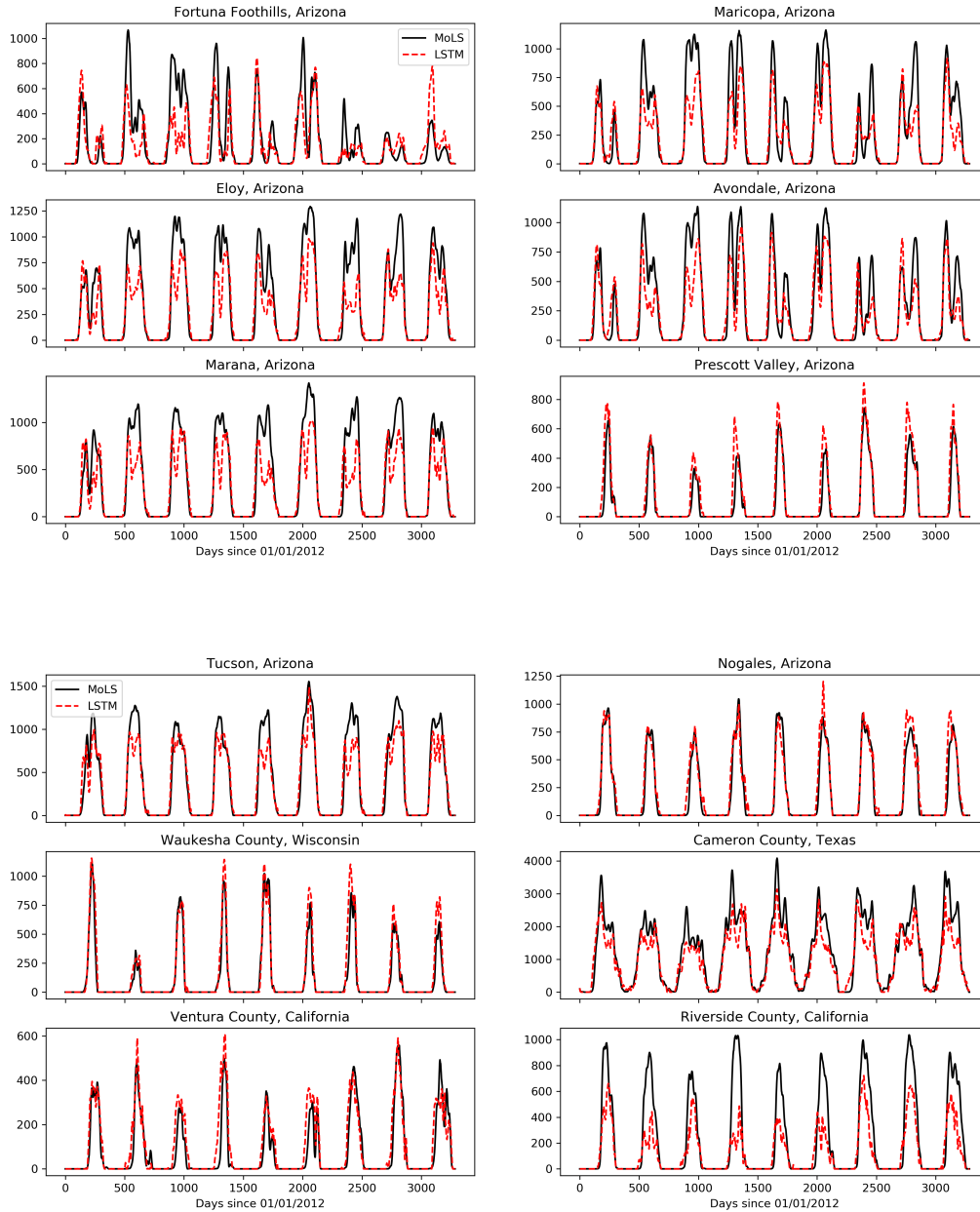
Table 13: Training and validation locations. \* locations are used in double peak oversampling. States and locations are organized alphabetically.

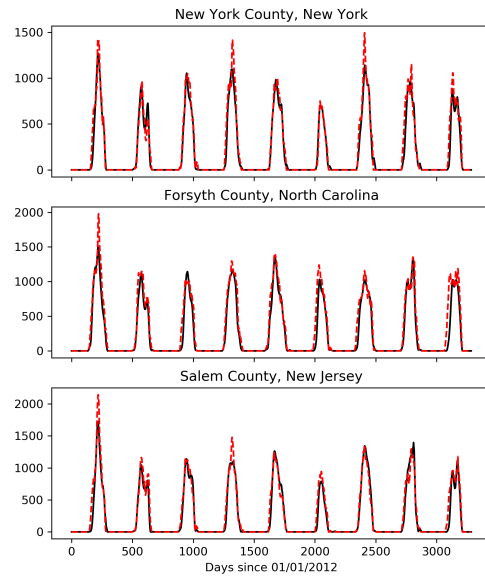
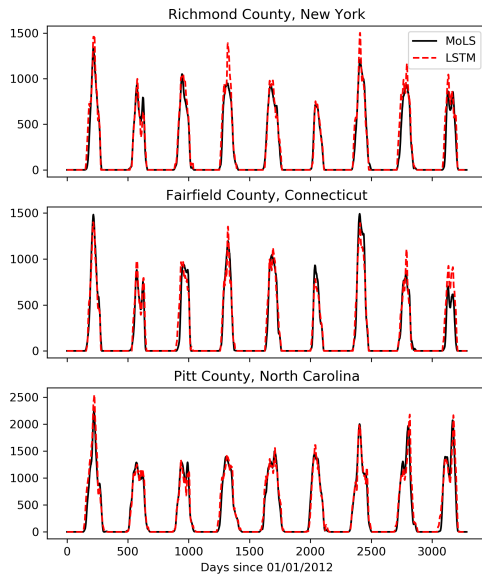
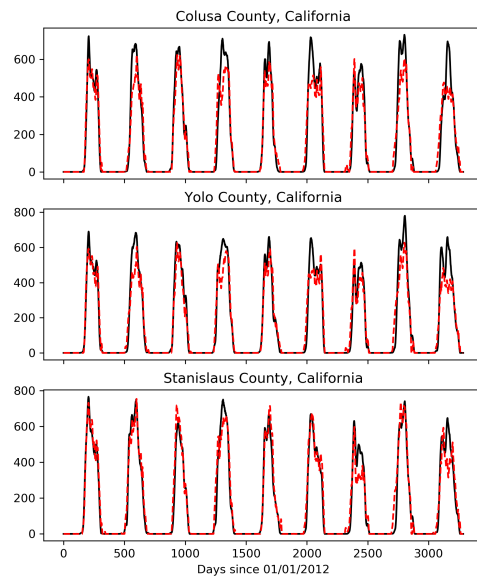
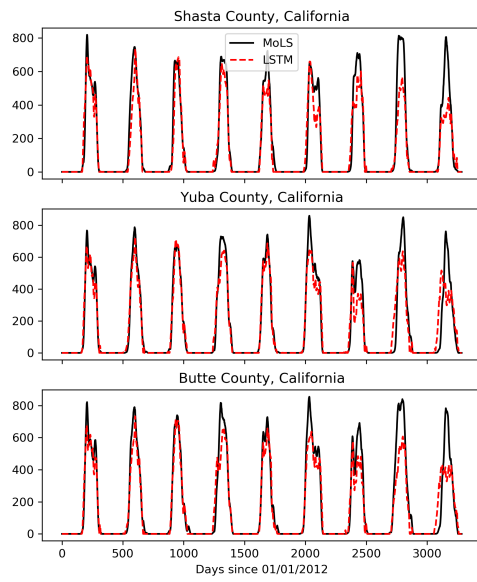
<b>State</b>	<b>Testing Locations</b>
Florida (Counties)	Jackson, Osceola, Collier, Pinellas
New Jersey (Counties)	Salem, Essex
North Carolina (Counties)	Forsyth, Pitt
Connecticut (Counties)	Fairfield
New York (Counties)	Richmond, New York
California (Counties)	Ventura, Riverside, Shasta, Colusa, Yuba, Yolo, Butte, Stanislaus
Texas (Counties)	Cameron
Wisconsin (Counties)	Waukesha
Arizona (Cities)	Fortuna Foothills, Maricopa, Eloy, Avondale, Marana, Prescott Valley, Tucson, Nogales

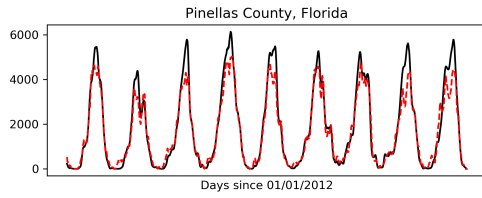
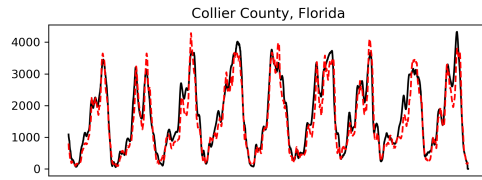
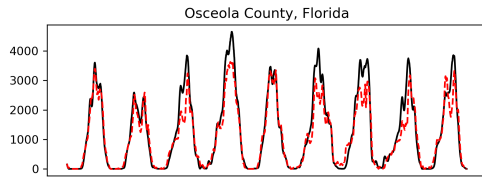
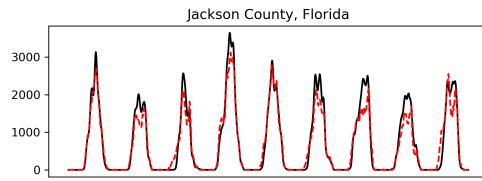
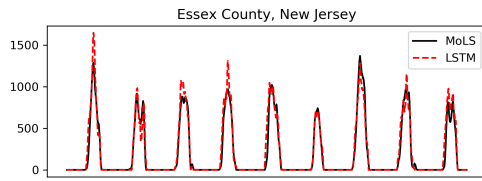
Table 14: Testing locations. States are organized bottom to top by their performance on the combined metric and locations within each state are organized left to right in the order they appear in Figure 6.

## Supplementary Material - MoLS-LSTM Comparison

The figures below show how the predictions of the LSTM model compare to MoLS data over a period of 9 years (2012-2020). Each panel corresponds to one column of Figure 6 and the locations are in the same order as in Figure 6.







## References

- [1] A. Krizhevsky, I. Sutskever, and G. E. Hinton, “ImageNet classification with deep convolutional neural networks,” Advances in Neural Information Processing Systems, vol. 25, pp. 1097–1105, 2012.
- [2] D. Kwon, H. Kim, J. Kim, S. C. Suh, I. Kim, and K. J. Kim, “A survey of deep learning-based network anomaly detection,” Cluster Computing, pp. 1–13, 2019.
- [3] T. H. Nguyen, K. Cho, and R. Grishman, “Joint event extraction via recurrent neural networks,” in Proceedings of the 2016 Conference of the North American Chapter of the Association for Computational Linguistics: Human Language Technologies, pp. 300–309, 2016.
- [4] J. Schmidhuber, “Deep learning in neural networks: An overview,” Neural Networks, vol. 61, pp. 85–117, 2015.
- [5] “Maca datasets.”  
<http://www.climatologylab.org/maca.html>. The climate forcings in the MACAv2-METDATA were drawn from a statistical downscaling of global climate model (GCM) data from the Coupled Model Intercomparison Project 5 [29] utilizing the Multivariate Adaptive Constructed Analogs [30] method with the METDATA [31] observational dataset as training data.
- [6] J. Lega, H. E. Brown, and R. Barrera, “*Aedes aegypti* (Diptera: Culicidae) abundance model improved with relative humidity and precipitation-driven egg hatching,” Journal of Medical Entomology, vol. 54, no. 5, pp. 1375–1384, 2017.
- [7] World Health Organization and UNICEF, “Global vector control response 2017-2030,” 2017.
- [8] A. Ong, M. Sandar, M. I. Chen, and L. Y. Sin, “Fatal dengue hemorrhagic fever in adults during a dengue epidemic in Singapore,” International Journal of Infectious Diseases, vol. 11, no. 3, pp. 263–267, 2007.
- [9] S. Cauchemez, M. Ledrans, C. Poletto, P. Quenel, H. de Valk, V. Colizza, and P. Y. Boalle, “Local and regional spread of chikungunya fever in the Americas,” Eurosurveillance, vol. 19, no. 28, 2014.
- [10] J. Heukelbach, C. H. Alencar, A. A. Kelvin, W. K. de Oliveira, and L. P. de Góes Cavalcanti, “Zika virus outbreak in Brazil,” The Journal of Infection in Developing Countries, vol. 10, no. 02, pp. 116–120, 2016.
- [11] E.-E. Ooi, K.-T. Goh, and D. J. Gubler, “Dengue prevention and 35 years of vector control in Singapore,” Emerging Infectious Diseases, vol. 12, no. 6, p. 887, 2006.
- [12] R. Barrera, V. Acevedo, G. E. Felix, R. R. Hemme, J. Vazquez, J. L. Munoz, and M. Amador, “Impact of autocidal gravid ovitraps on chikungunya virus incidence in



- Aedes aegypti* (Diptera: Culicidae) in areas with and without traps,” Journal of Medical Entomology, vol. 54, no. 2, pp. 387–395, 2017.
- [13] World Health Organization, “Mosquito (vector) control emergency response and preparedness for Zika virus. 2016,” Geneva: WHO, 2016.
- [14] P. A. Ryan, D. Alsemgeest, M. L. Gatton, and B. H. Kay, “Ross River virus disease clusters and spatial relationship with mosquito biting exposure in Redland Shire, Southern Queensland, Australia,” Journal of Medical Entomology, vol. 43, p. 1042–1059, 2006.
- [15] S. Guo, F. Ling, J. Hou, J. Wang, G. Fu, and Z. Gong, “Mosquito surveillance revealed lagged effects of mosquito abundance on mosquito-borne disease transmission: a retrospective study in Zhejiang, China,” PLoS One, vol. 9, p. e112975, 2014.
- [16] M. U. Kraemer, M. E. Sinka, K. A. Duda, A. Q. Mylne, F. M. Shearer, C. M. Barker, C. G. Moore, R. G. Carvalho, G. E. Coelho, W. Van Bortel, et al., “The global distribution of the arbovirus vectors *Aedes aegypti* and *Ae. albopictus*,” eLife, vol. 4, p. e08347, 2015.
- [17] J. Rocklöv and R. Dubrow, “Climate change: an enduring challenge for vector-borne disease prevention and control,” Nature Immunology, vol. 21, no. 5, pp. 479–483, 2020.
- [18] M. Kamal, M. A. Kenawy, M. H. Rady, A. S. Khaled, and A. M. Samy, “Mapping the global potential distributions of two arboviral vectors *Aedes aegypti* and *Ae. albopictus* under changing climate,” PloS One, vol. 13, no. 12, p. e0210122, 2018.
- [19] J. P. Messina, M. U. Kraemer, O. J. Brady, D. M. Pigott, F. M. Shearer, D. J. Weiss, N. Golding, C. W. Ruktanonchai, P. W. Gething, E. Cohn, J. S. Brownstein, K. Khan, A. J. Tatem, T. Jaenisch, C. J. Murray, F. Marinho, T. W. Scott, and S. I. Hay, “Mapping global environmental suitability for Zika virus,” eLife, vol. 5, p. e15272, 2016.
- [20] C. W. Morin and A. C. Comrie, “Modeled response of the West Nile virus vector *Culex quinquefasciatus* to changing climate using the dynamic mosquito simulation model,” International Journal of Biometeorology, vol. 54, no. 5, pp. 517–529, 2010.
- [21] R. Maciel-de Freitas, C. Torres Codeço, and R. Lourenço-de Oliveira, “Daily survival rates and dispersal of *Aedes aegypti* females in Rio de Janeiro, Brazil,” The American Journal of Tropical Medicine and Hygiene, vol. 76, pp. 659–665, 2007.
- [22] “CDC *Aedes* Challenge.”  
<https://predict.cdc.gov/post/5c4f6d687620e103b6dcd015>.
- [23] I. Goodfellow, Y. Bengio, and A. Courville, Deep Learning, vol. 1. MIT Press Massachusetts, USA:, 2017. <http://www.deeplearningbook.org>.
- [24] H. E. Brown, C. Smith, and S. Lashway, “Influence of the length of storage on *Aedes aegypti* (Diptera: Culicidae) egg viability,” Journal of Medical Entomology, vol. 54, pp. 489–491, 2017.

- [25] D. P. Kingma and J. Ba, “Adam: A method for stochastic optimization,” arXiv preprint arXiv:1412.6980, 2014.
- [26] S. J. Orfanidis, Introduction to Signal Processing. Prentice-Hall, Inc., 1995.
- [27] E. Eccel, “Estimating air humidity from temperature and precipitation measures for modelling applications,” Meteorological Applications, vol. 19, no. 1, pp. 118–128, 2012.
- [28] R. Hardwick Jones, S. Westra, and A. Sharma, “Observed relationships between extreme sub-daily precipitation, surface temperature, and relative humidity,” Geophysical Research Letters, vol. 37, no. 22, 2010.
- [29] K. E. Taylor, R. J. Stouffer, and G. A. Meehl, “An overview of CMIP5 and the experiment design,” Bulletin of the American Meteorological Society, vol. 93, no. 4, pp. 485–498, 2012.
- [30] J. T. Abatzoglou and T. J. Brown, “A comparison of statistical downscaling methods suited for wildfire applications,” International Journal of Climatology, vol. 32, no. 5, pp. 772–780, 2012.
- [31] J. T. Abatzoglou, “Development of gridded surface meteorological data for ecological applications and modelling,” International Journal of Climatology, vol. 33, no. 1, pp. 121–131, 2013.